Explicit Modeling and Optimization of Acoustic Metalenses for Baffled Sources

Théo Cavalieri,[1,*,†] Vicent Romero-García,[1,‡] Manuel Melon,[1] Jean-Philippe Groby,[1] and Jean-Christophe Chamard[2]

[1] *Laboratoire d'Acoustique de l'Université du Mans, UMR 6613, Institut d'Acoustique Graduate School, CNRS, Le Mans Université, Avenue Olivier Messiaen, 72085 Le Mans, France*

[2] *Stellantis, Centre Technique Vélizy, Route de Gisy, 78943 Vélizy-Villacoublay Cedex, France*

(Received 10 February 2023; revised 13 June 2023; accepted 15 June 2023; published 4 August 2023)

The steering and the focusing of acoustic beams are of increasing interest for personalized-sound-zone applications. Sound zones require the generation of a strong contrast in sound pressure level between different regions of the space. A way to do so is to control and steer the acoustic field radiated from a source with use of metamaterial-based acoustic lenses. Predictive models based on numerical approaches such as the finite-element method are commonly used, but they are generally cumbersome and time-consuming. In contrast, explicit models rely on Snell's law of refraction and phase gratings but do not account for the couplings between the metamaterial atoms. In this work, a metamaterial-based acoustic lens is proposed as a solution to steer and focus acoustic sources, with use of slits loaded with periodic Helmholtz resonators. We control the radiation of a baffled duct by a metalens located at the output of the waveguide and excited at the other end by a loudspeaker. A fully explicit two-dimensional predictive model is developed on the basis of the mode-matching technique, accounting for thermoviscous losses, interslit evanescent coupling, and high-order modes in the baffled duct. The pressure radiated by the metalens outside the baffled duct is then explicitly derived. The semianalytical results show excellent agreement when compared with the solutions obtained by the finite-element method, both in the near field and in the far field over a wide frequency range. An optimization strategy is then proposed, and the beam steering and focusing are reported experimentally on a three-dimensionally-printed prototype.

DOI: 10.1103/PhysRevApplied.20.024012

I. INTRODUCTION

Recently, the possibility to create and control acoustic sound zones has been of growing interest [1–4]. Sound zones require the creation of a contrast in sound pressure level (SPL) between distinct regions of the space. Such applications have already been addressed with use of active (electromechanoacoustic) solutions [1,5], but passive acoustic structures can also establish high SPL contrast by confining acoustic energy in some regions of space while maintaining low amplitudes in other regions. Acoustic lenses are of interest in this latter case. While active solutions require additional sources of electrical power, passive solutions are purely based on a structured treatment and require no additional sources of energy. Both the growing prospective applications of acoustic metamaterials and the elementary nature of passive acoustic lenses initiated the need for modeling tools. Numerical simulations are generally more suitable than analytical models at solving complex problems, but are often accompanied by high computational costs. However, a well-designed analytical model can provide accurate results in a short time. This is especially efficient for the rapid optimization and design of acoustic solutions and treatments.

In most of the scientific literature, acoustic lenses are modeled either numerically or explicitly with use of phase arrays [6,7]. Snell's law of refraction is valid when the phase gradient is continuous, i.e., the propagation medium itself has no discontinuities. However, the assumption of a continuous gradient of phase has to be questioned in the case of discrete structures, which are particularly common in the field of metamaterials [8,9]. The motivation for this work is to propose a complete explicit model for metamaterial-based acoustic lenses that does not rely on phase gradients but rather relies on a "mode-matching" (MM) approach [10]. This method also has the advantage of accounting for the couplings between the metamaterial and its host waveguide, as preliminary studies related to this work evidenced the need to account for high-order modes and interslit couplings to accurately

*theo.cavalieri@empa.ch and tcaval@univ-lemans.fr

†Present address: EMPA—Swiss Federal Laboratories for Materials Science and Research, Überlandstrasse 129, 8600 Dübendorf, Switzerland.

‡Present address: Instituto Universitario de Matemática Pura y Aplicada, Universitat Politècnica de València, Camino de Vera s/n, 46022 Valencia, Spain.

predict the acoustic radiation of the metalens. A validation study is available in Supplemental Material [11], proving the capability of the explicit model to accurately predict the acoustic behavior of metalenses when compared with finite-element-method (FEM) results.

In this work, an array of slits loaded with Helmholtz resonators constitutes the metalens. Such a geometry offers much flexibility as all the dimensions of both the slits and the resonators can be independently tuned. An optimization procedure is proposed so as to steer the acoustic beam at the outlet of the baffled duct. The optimization relies on the explicit expressions and uses model-order-reduction techniques [12] and the particle-swarm-optimization (PSO) algorithm [13,14]. The width of the slits and the geometry of the resonators are continuously graded according to a polynomial description and are meant to provide acoustic beam steering at a specific angle. The metalens with optimal geometry is then fabricated by additive-manufacturing processes [15,16] and tested experimentally in an anechoic chamber. This work paves the way for a complete analytical tool for the optimization of the radiation of acoustic lenses using metamaterials. Furthermore, the architecture of the present predictive model can be extended to design 3D metamaterials.

This article is organized as follows: First the principles of Snell's law of refraction and phase arrays are recalled in Sec. II. Then the geometry of the metalens and the problem of acoustic wave propagation and radiation is presented in Sec. III, for which explicit and numerical solutions are proposed in Sec. IV. The metalens is optimized for a beam-steering configuration as detailed in Sec. V. This optimal configuration is then studied experimentally in Sec. VI, and all the results are presented in Sec. VII. The conclusions, limitations, and perspectives of this work are discussed in Sec. VIII. A more-detailed description of the underlying physics and mathematics on which this work is based is provided in Supplemental Material [11].

II. REFRACTION-BASED ACOUSTIC LENSES

Introduced independently by Snell and Descartes in the 17th century, the refraction law states the relationship between the angles of the incident and refracted waves at the interface between two media [17]. It is now well established in the literature that it is possible to deviate—steer—an acoustic wave with use of a gradient of phase. This is achievable by use of heterogeneous media having space-dependent sound speed [6]. Consider a medium bounded by two interfaces Γ_0 and Γ_L with a graded phase $\Phi(x_1)$ along its vertical direction $\hat{\mathbf{e}}_1$, as shown in Fig. 1. The generalized Snell's law gives the relation between the incident and refracted angles [18] at the position x_1 as

$$\sin(\theta_t(x_1)) = \frac{1}{k_0}\frac{d\Phi}{dx_1} + \sin(\theta_i(x_1)), \tag{1}$$

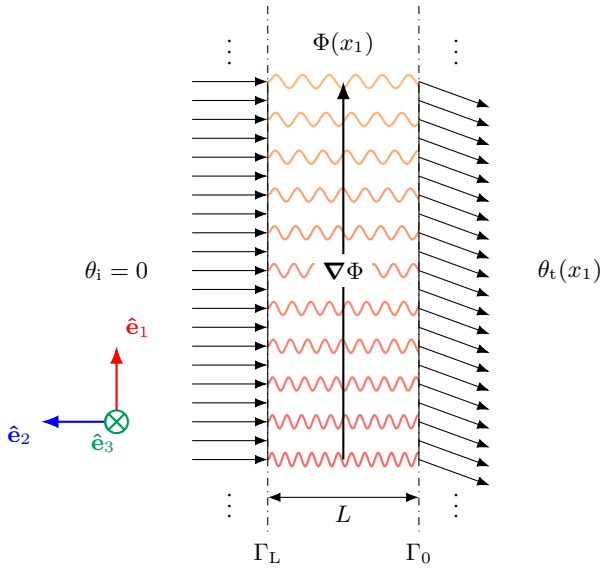

FIG. 1. Conceptual representation of Snell's law where a layer is bounded by two interfaces Γ_0 and Γ_L with a graded phase $\phi(x_1)$ along its vertical direction $\hat{\mathbf{e}}_1$. The incident and refracted angles are shown on either side of the layer by black arrows.

where $\theta_t(x_1)$ and $\theta_i(x_1)$ are the angles of refraction and incidence, respectively, and $k_0 = \omega/c_0$ is the wave number of the surrounding medium, with $\omega = 2\pi f$ the angular frequency and c_0 the sound speed in a free field. Considering a normal plane wave, i.e., $\theta_i = 0$, and the phase function $\Phi(x_1) = \omega L/c(x_1)$, we obtain

$$\sin(\theta_t(x_1)) = Lc_0\frac{d}{dx_1}\left(\frac{1}{c(x_1)}\right), \tag{2}$$

where L is the thickness of the layer. Hence, the properties of the heterogeneous layer can be tuned so as to grade the phase at Γ_0. Different types of sound-speed profiles can be designed depending on the desired effect [6].

III. SLITS AND HELMHOLTZ RESONATORS AS ACOUSTIC METALENSES

The acoustic propagation problem is set in the 2D Cartesian coordinate system with unit vectors $\hat{\mathbf{e}}_i$ and the position vector given by $\mathbf{x} = (x_1, x_2) \in \mathbb{R}^2$ as sketched in Fig. 2. First, a semi-infinite waveguide of height $w^{(0)}$ is considered and is represented by the domain $\Omega^{(0)}$. Then, the metalens made of slits and Helmholtz resonators is positioned at one end of the main waveguide and is represented by the domain Ω_π. The interface between the main waveguide $\Omega^{(0)}$ and the metalens Ω_π located at $x_2 = L$ is denoted Γ_L. The metalens itself is composed of N parallel slits denoted by the domains $\Omega_S^{(n)}$, and $d^{(n)}$ and $w^{(n)}$ are, respectively, the lowest position and the width of the nth slit along the direction $\hat{\mathbf{e}}_1$; see the inset in Fig. 2.

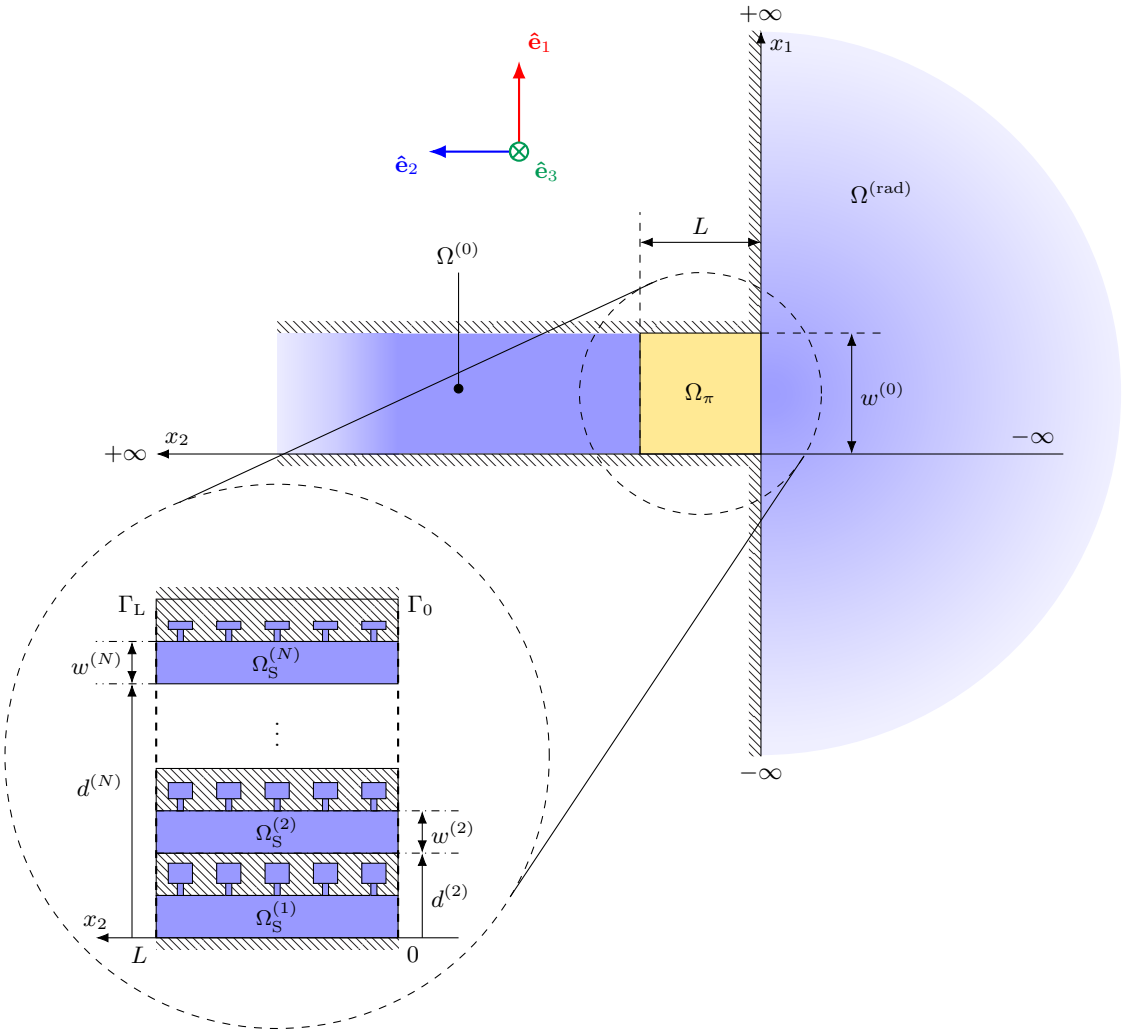

FIG. 2. Sketch of the 2D system. The waveguide $\Omega^{(0)}$ and exterior domain $\Omega^{(\mathrm{rad})}$ are in shaded blue, and the resonant metalens Ω_π is shown in yellow. The enlarged view shows a sketch of the slits and periodic resonators within the metalens Ω_π.

The set of slits is introduced by $\mathcal{N} = \{1, \ldots, N\} \subset \mathbb{N}^\star$. The duct and the metalens are baffled at $x_2 = 0$ and radiate in a semi-infinite half-space shown as a semicircle on the right-hand side of Fig. 2. The half-space is connected to the other end of the slits and is simply denoted by the domain $\Omega^{(\mathrm{rad})}$.

The interface between the slits and the half-space at $x_2 = 0$ is Γ_0. Both interfaces contain $\Gamma_\mathrm{L}^{(n)}$ and $\Gamma_0^{(n)}$, to make the distinction between the open and closed boundaries at both ends of the metamaterial, as detailed in Eq. (3). Finally, each slit is loaded with Q identical and evenly spaced Helmholtz resonators (with spacing b_uc; uc refers to unit-cell); the Helmholtz resonators may differ from one slit to another. A slit loaded with Helmholtz resonators is shown in Fig. 3. The wave propagation in the slits $\Omega_\mathrm{S}^{(n)}$ is governed by the geometric features of the resonant periodic structure. Consider $\mathcal{Q} = \{1, \ldots, Q\} \subset \mathbb{N}^\star$ the set of Helmholtz resonators parallel to the nth slit. The qth resonator is made of a neck $\Omega_{\mathrm{N},q}^{(n)}$ and a cavity $\Omega_{\mathrm{C},q}^{(n)}$. Thus, each resonator is defined by the domain $\Omega_{\mathrm{H},q}^{(n)}$. Moreover, the portions of the slits before and after the resonators are denoted $\Omega_{\mathrm{S},+}^{(n)}$ and $\Omega_{\mathrm{S},-}^{(n)}$, respectively, and are shown in light orange in Fig. 3. These sub-slits have length $b_+^{(n)}$ and $b_-^{(n)}$. Albeit, the dimensions of the entire slits satisfy $L := b_+^{(n)} + (Q-1)b_\mathrm{uc} + b_-^{(n)}$. In a more-formal way, the domains that describe the geometry of the system satisfy

$$
\begin{aligned}
\Omega^{(0)} &= \left\{\mathbf{x} \in \mathbb{R}^2 \mid x_2 \geq L, x_1 \in \left[0, w^{(0)}\right]\right\}, \\
\Omega_\mathrm{S}^{(n)} &= \left\{\mathbf{x} \in \mathbb{R}^2 \mid x_2 \in [0, L], x_1 \in \left[d^{(n)}, d^{(n)} + w^{(n)}\right]\right\}, \\
\Omega^{(\mathrm{rad})} &= \left\{\mathbf{x} \in \mathbb{R}^2 \mid x_2 \leq 0\right\}, \\
\Omega_{\mathrm{H},q}^{(n)} &= \Omega_{\mathrm{N},q}^{(n)} \cup \Omega_{\mathrm{C},q}^{(n)},
\end{aligned}
\tag{3}
$$

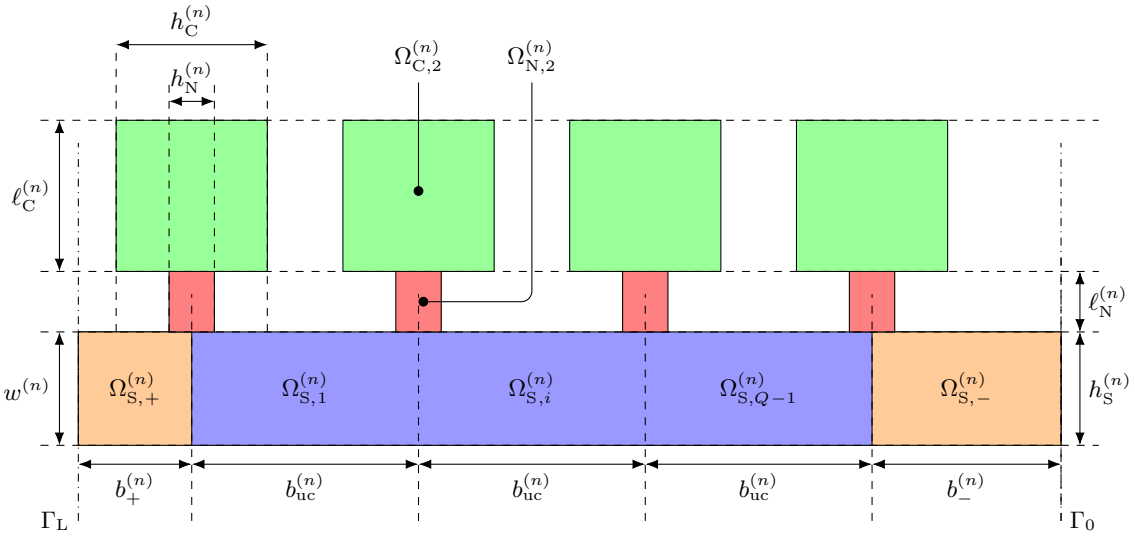

FIG. 3. Sketch of the Helmholtz resonators mounted onto a single slit. The slit $\Omega_{\mathrm{S}}^{(n)}$ is shown in blue, its start and end subslits are shown in orange, the cavities are shown in green, and the necks are shown in red.

and the interfaces are given by

$$\begin{aligned}\Gamma_{\mathrm{L}} &= \Omega^{(0)} \cap \Omega_{\pi},\\ \Gamma_0 &= \Omega^{(\mathrm{rad})} \cap \Omega_{\pi},\\ \Gamma_{\mathrm{L}}^{(n)} &= \Omega^{(0)} \cap \Omega_{\mathrm{S}}^{(n)},\\ \Gamma_0^{(n)} &= \Omega^{(\mathrm{rad})} \cap \Omega_{\mathrm{S}}^{(n)}.\end{aligned} \tag{4}$$

IV. EXPLICIT AND NUMERICAL MODELING

In this section, two different modeling approaches are presented. The first one constitutes the analytical model and uses modal projection to obtain the pressure and velocity at the end of each slit, while the FEM is used as a validation of the aforementioned analytical model. Extensive details are provided in Supplemental Material [11].

A. Mode-matching techniques

Acoustic wave propagation under normal temperature and pressure is assumed, in the linear domain with Fourier time convention $e^{-i\omega t}$. Thus, the time dependence of the acoustic fields is omitted in the following statements. An incident plane wave in the main duct $\Omega^{(0)}$ propagating along the direction $-\hat{\mathbf{e}}_2$ is considered. The pressure field is denoted p and the particle velocity vector is denoted $\mathbf{v} = (v_1, v_2)$. The pressure field in the domain $\Omega^{(0)}$ is given by the infinite sum of all modal components along $\hat{\mathbf{e}}_1$ and the general Green's formulation is used in the half-space $\Omega^{(\mathrm{rad})}$:

$$p^{(0)}(\mathbf{x},\omega) = \sum_{m\in\mathbb{N}} \cos\left(k_{1,m}^{(0)} x_1\right) \times \left[\delta_m e^{-ik_{2,m}^{(0)}(x_2-L)} + R_m e^{ik_{2,m}^{(0)}(x_2-L)}\right], \tag{5a}$$

$$p^{(\mathrm{rad})}(\mathbf{x},\omega) = \int_{-\infty}^{+\infty} T^{(\mathrm{rad})}\left(k_1^{(\mathrm{rad})},\omega\right)\left[e^{ik_1^{(\mathrm{rad})}x_1 - ik_2^{(\mathrm{rad})}x_2}\right] \times \frac{dk_1^{(\mathrm{rad})}}{k_2^{(\mathrm{rad})}}, \tag{5b}$$

with δ_m the Kronecker δ ($\delta_0 = 1$ defines the incident plane wave), and the wave vectors satisfy

$$\mathbf{k}_m^{(0)} = \left(\frac{m\pi}{w^{(0)}}, \sqrt{\left(k^{(0)}\right)^2 - \left(\frac{m\pi}{w^{(0)}}\right)^2}\right)^{\top}, \tag{6a}$$

$$k_2^{(\mathrm{rad})} = \left(\left(k^{(\mathrm{rad})}\right)^2 - \left(k_1^{(\mathrm{rad})}\right)^2\right)^{1/2}, \tag{6b}$$

such that their real part satisfies $\mathrm{Re}\left(k_{2,m}^{(0)}\right) \geq 0$, and $\mathrm{Re}\left(k^{(\mathrm{rad})}\right) \geq 0$. The superscript $\top$ denotes the nonconjugated transposition. In Eq. (5a), R_m represents the reflection coefficient of the mth mode of the duct at the interface Γ_{L}. Within each slit $\Omega_{\mathrm{S}}^{(n)}$, only the propagation of plane waves is assumed since their dimension along $\hat{\mathbf{e}}_1$ is considered much smaller than the half-wavelength at the maximum frequency of interest. The pressure and normal velocity at both ends are thus linked by the corresponding transfer matrix [19–23]:

$$\begin{pmatrix} p^{(n)} \\ \tilde{v}_2^{(n)} \end{pmatrix}_L = \mathbf{T}^{(n)} \begin{pmatrix} p^{(n)} \\ \tilde{v}_2^{(n)} \end{pmatrix}_0. \tag{7}$$

Here the volume flow $\tilde{v}_2^{(n)} = S^{(n)}[\hat{\mathbf{e}}_2 \cdot \mathbf{v}^{(n)}]$ is considered, with $S^{(n)}$ the cross-section area of each slit ($S^{(n)} = w^{(n)}$ in two dimensions). The matrix $\mathbf{T}^{(n)} \in \mathbb{C}^{2\times 2}$ is the transfer

matrix that connects the state vectors at both interfaces and accounts for thermal and viscous losses within the slits and resonators, as well as the radiation corrections at the discontinuities in the resonator and between the resonator and the slit [24,25]. At both interfaces Γ_{L} and Γ_0 the continuity of the acoustic pressure and normal velocity is assumed and satisfies for all $n \in \mathcal{N}$

$$\begin{aligned} p^{(0)} &= p_L^{(n)} \quad \text{for all } x_1 \in \Gamma_{\mathrm{L}}^{(n)}, \\ v_2^{(0)} &= v_2^{(n)} \quad \text{for all } x_1 \in \Gamma_{\mathrm{L}}^{(n)}, \\ v_2^{(0)} &= 0 \quad \text{for all } x_1 \in \Gamma_{\mathrm{L}} \setminus \Gamma_{\mathrm{L}}^{(n)}, \end{aligned} \qquad \begin{aligned} p^{(\mathrm{rad})} &= p_0^{(n)} \quad \text{for all } x_1 \in \Gamma_0^{(n)}, \\ v_2^{(\mathrm{rad})} &= v_2^{(n)} \quad \text{for all } x_1 \in \Gamma_0^{(n)}, \\ v_2^{(\mathrm{rad})} &= 0 \quad \text{for all } x_1 \in \Gamma_0 \setminus \Gamma_0^{(n)}. \end{aligned} \tag{8}$$

As the transfer-matrix method (TMM) is applicable only for plane waves in the slits, the acoustic pressure field is assumed to be constant along x_1 on $\Gamma_0^{(n)}$ and $\Gamma_{\mathrm{L}}^{(n)}$ such that

$$\begin{aligned} p_L^{(n)} w^{(n)} &= \int_{\Gamma_{\mathrm{L}}^{(n)}} p^{(n)} dx_1, \\ p_0^{(n)} w^{(n)} &= \int_{\Gamma_0^{(n)}} p^{(n)} dx_1. \end{aligned} \tag{9}$$

The continuity equations for acoustic pressure and particle velocity at both interfaces are projected onto the modes of the main duct, the plane mode of the slits, and the Green's integral formulation for radiation in the half-space. After matching the modal amplitudes and using the TMM, a system of coupled linear equations is obtained and cast into the form $\mathbf{Hb} = \mathbf{s}$, with $\mathbf{H}$ a matrix of size $2N \times 2N$. Inverting the system provides the pressures and particle velocities at the end of each slit as a unique solution to the vector of unknowns:

$$\mathbf{b} = \left(p_0^{(1)}, \ldots, p_0^{(N)}, v_2^{(1)} \Big|_0, \ldots, v_2^{(N)} \Big|_0 \right)^{\top}. \tag{10}$$

The complete analytical model is as follows: once the geometry is set, the losses within each subdomain of Ω_π are computed, and then the TMM is applied. Finally the matrix $\mathbf{H}$ is built and inverted.

B. Numerical validation with the FEM

To first validate the results of the explicit model, finite-element simulations of the acoustic propagation problem are performed. The simulations are performed with COMSOL MULTIPHYSICS. The geometry presented in Sec. III is implemented and an incident plane wave is imposed in the main duct $\Omega^{(0)}$. To satisfy the Sommerfeld radiation condition [26,27] for $x_2 < 0$, perfectly matched layers are implemented [28] and surround the half-space $\Omega^{(\mathrm{rad})}$. Neumann boundary conditions are applied to all boundaries of the metalens and to those of the baffled duct. The acoustic thermal and viscous dissipation in Ω_π is accounted for with use of the effective complex and frequency-dependent wave number and characteristic impedance [25]. The mesh of the finite-element model is adapted to be finer in narrow regions, i.e., mainly in the resonators and around the interfaces Γ_{L} and Γ_0. The simulation is performed with at least ten elements per wavelength. The FEM solution provides the acoustic pressure and particle velocity fields at all points in the main duct, in the metalens, and in the half-space.

For a metalens comprising $N = 10$ slits each loaded with $Q = 5$ resonators, the analytical model solves the problem for $N_{\mathrm{f}} = 100$ frequencies in 142 s, while the same problem with the FEM takes around 200 s on a common laptop (MacBook Pro 13 in., 2017, macOS 10.13.6, Intel Core i7 at 2.5 GHz, 16 GB RAM at 2133 MHz) running in MATLAB. However, the performances of both models can differ greatly depending on the number of slits, the truncation of sums and integrals, the FEM mesh refinement, and so on. Although the time difference presented here does not appear to be significant, it becomes predominant for optimization over short frequency bands, particularly because of the meshing time with the FEM. Finally, as the systems of equations are independent for each frequency, the whole process could be easily done with parallel computing.

C. Acoustic radiation

On the one hand, the far-field acoustic radiation of the system is obtained from the spatial Fourier transform of the acoustic normal velocity $v_2^{(0)}$ at the end of the slits, i.e., at the interface Γ_0. The far-field directivity function $D(\theta)$ is introduced as

$$D(\theta) = -i \frac{\rho \omega^2}{2\pi} \int_{\Gamma_0} [\hat{\mathbf{e}}_2 \cdot \mathbf{v}(x_1)]\, e^{-ik_0 \sin(\theta) x_1}\, dx_1, \tag{11}$$

with $x_1 \in \Gamma_0$, and the far-field radiated pressure $p^{(\mathrm{far})}(r, \theta) = (1/r) e^{ik_0 r} D(\theta)$ [29]. Here θ denotes the angle from $\hat{\mathbf{e}}_2$ to $\hat{\mathbf{e}}_1$, and the distance from the origin $r = |\mathbf{x}|$.

On the other hand, the near-field radiated acoustic pressure is calculated from the integral formulation given in Eq. (5b), which has infinite bounds, and singularities of the denominator have to be excluded. Using properties of

symmetry and changes of variables, one can solve for the radiated pressure $p^{(\mathrm{rad})}$ with good accuracy. A complete validation study is proposed in Supplemental Material [11] for different test cases. The analytical results and the FEM results are in excellent agreement as long as the waves propagating in the slits are in the plane-wave regime. The numerical errors essentially come from the truncation of the high-order modes and radiation integrals, as well as additional couplings within the resonators that are not accounted for. More details are also given regarding the derivation of the directivity function, the near-field radiation integrals, and the transmission loss of the system.

V. OPTIMIZATION OF THE METALENS

To control the far-field directivity of the metalens, its inner geometry has to be adapted. Thus, the analytical model serves as a kernel in an optimization problem. This leads to optimization of all possible individual parameters of the slits and of the resonators. Here the commonly used downhill simplex method (also known as the Nelder-Mead algorithm [30]) is unpractical because of the high number of parameters to optimize. To tackle this problem and to provide a fast and efficient minimization procedure, the number of parameters is reduced with use of polynomial interpolation and a proper minimization method is chosen.

A. Cost function and minimization strategy

It is common for some optimization procedures to define a cost function that is to be minimized, resulting in refinement of the parameters of the system at each iteration. Probably the most-convenient and most-intuitive procedure in the actual context is to specify a shifted Gaussian curve as the objective far-field directivity D_{obj}. Thus, the objective function is defined as a lobe with

$$D^{\mathrm{obj}}(\theta) = \exp\left[-\frac{\left(\theta-\theta_{\mathrm{obj}}\right)^2}{2\sigma^2}\right], \tag{12}$$

where $\theta_{\mathrm{obj}} \in [-\pi/2, \pi/2]$ is the angle where the directivity function is maximal and σ controls the width of the main lobe.

The cost function is defined as the quadratic error between D and the shifted Gaussian lobe D^{obj}, and is designed to inflict a strong penalty over the angle of maximal radiated pressure. This ensures the quadratic error is minimized while the steering angle $\theta_{\max} = \theta_{\mathrm{obj}}$ is reached. The cost function is cast into the form

$$J := |\theta_{\max} - \theta_{\mathrm{obj}}| + \frac{1}{N_\theta}\sum_{i=1}^{N_\theta}\left|D_i - D_i^{\mathrm{obj}}\right|^2, \tag{13}$$

with $N_\theta = 181$ the number of distinct angles between -90° and $+90^\circ$. A well-suited minimization routine for this problem is PSO [13,14]. The PSO converges towards a minimum of J relying on a herd of particles, at the position of which the cost function is evaluated. At each iteration, the position of each particle is updated on the basis of its previous steps and on the basis of the lowest values of J encountered by the herd in the search space. Such an optimization is not computationally heavy because computing J for each iteration is based on the explicit model, having a large number of function evaluations is not a burden. In the present case, the optimization is initialized with ten particles distributed in every dimension of the search space as adding particles strengthens the ability of the method to converge towards the global minimum.

B. Model order reduction using polynomials

Although having a high number of dimensions can be tackled using PSO, an additional technique is implemented to reduce the number of parameters (and computation time) while maintaining flexibility in the search space. This is provided by the $\mathcal{C}^1$-continuous piecewise cubic Hermite interpolating polynomials (PCHIPs), which preserve the monotonicity of the interpolated data [31]. Another approach would be the use of Bezier curves as they provide additional degrees of freedom and flexibility, but this is out of the scope of this work. For example, instead of optimizing the cavity length of the resonators independently across ten slits, only the values at slits 1, 5, and 10 are actually optimized, while the cavity lengths for the other slits are interpolated with use of PCHIPs. Thus, we can adjust the number of nodes for which the optimization is performed, as it impacts the possible geometric outcomes. The first node is at position $x_1 = 0$ and the last node is at position $x_1 = w^{(0)}$. Between them, the other nodes are placed at $x_1^{(i)} = (i-1)w^{(0)}/(N_{\mathrm{nodes}}-1)$, with $i \in \{1,\ldots,N_{\mathrm{nodes}}-1\}$. Along the interval $\left[x_1^{(i)}, x_1^{(i+1)}\right]$ between two nodes, each geometric parameter reads

$$\mathcal{W}^{(n)}(x_1) := \sum_{k=0}^{3} a_k \left(d^{(n)} + \frac{w^{(n)}}{2} - x_1^{(i)}\right)^k, \tag{14}$$

with a_k the weights of the polynomial interpolation function.

The extreme case of optimization for a single node implies all parameters will have the same value along $\hat{\mathbf{e}}_1$, resulting in a zero gradient $\hat{\mathbf{e}}_1 \cdot \nabla\mathcal{W}^{(n)} = 0$. With the use of two nodes, the possible profiles are affine and linear functions, i.e., they are monotonic and do satisfy $\hat{\mathbf{e}}_1 \cdot \nabla\mathcal{W}^{(n)} = \text{const.}$ (which implies an asymmetric geometry), but also include the nongraded (constant) cases as sole symmetric profiles. A total of three nodes can still provide nongraded and linear profiles, but yields much-richer symmetric and nonmonotonic profiles. To get a grip on the number of nodes that has to be used, we consider the following example.

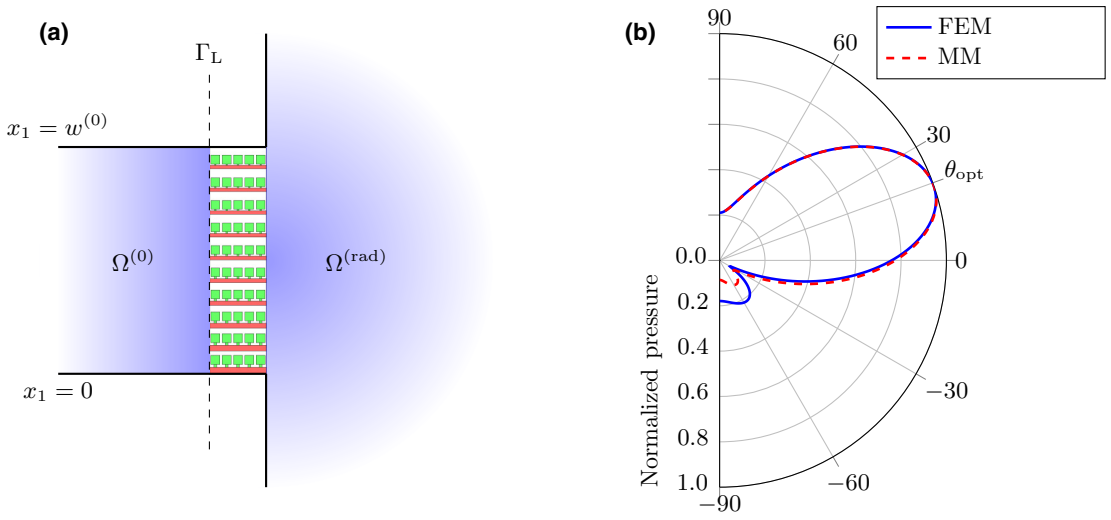

FIG. 4. (a) Optimal geometry of the metalens for $+20^\circ$ steering at $f_{opt} = 2$ kHz. (b) Far-field directivity diagram comparing the FEM results (solid blue line) and the results obtained with the explicit model (dashed red line).

The optimal geometry and far-field directivity of the metalens able to steer the acoustic beam by $\theta_{obj} = +20^\circ$ at frequency $f_{opt} = 2$ kHz are displayed in Fig. 4. We observe good agreement of the absolute pressure between the analytical model and the FEM. Some discrepancies can still be noticed and are linked to the normal velocity profile along Γ_0. The analytical solution of velocity is piecewise constant, while the FEM solution is continuous, and truncation errors in the analytical model also come into play. The results are produced with use of the PCHIP interpolation with $N_{nodes} = 3$. The geometry is set with a main duct of height $w^{(0)} = 20$ cm and the thickness of the metalens is $L = 5$ cm, comprising $N = 10$ slits, each of them loaded with $Q = 5$ Helmholtz resonators. The chosen

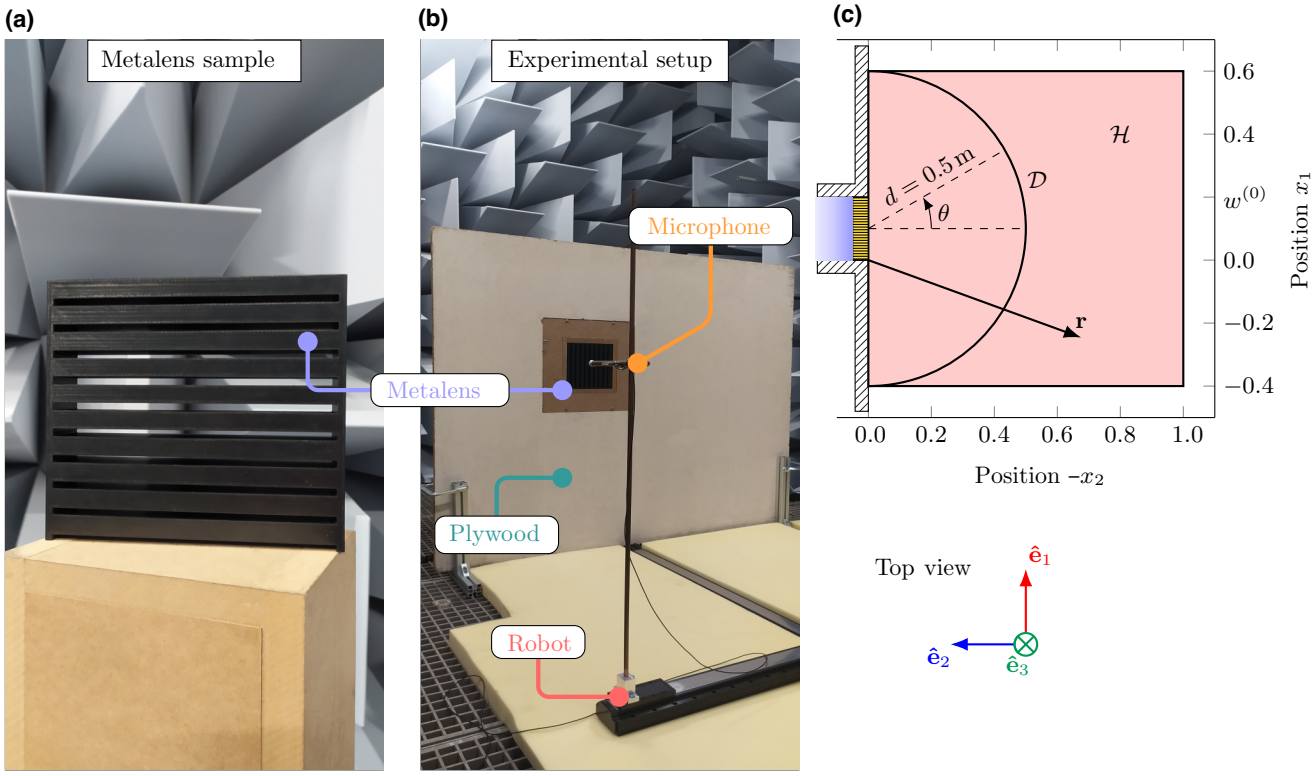

FIG. 5. (a) Photograph of the sample and (b) global view of the experimental setup. (c) Sketch of the probed domains.

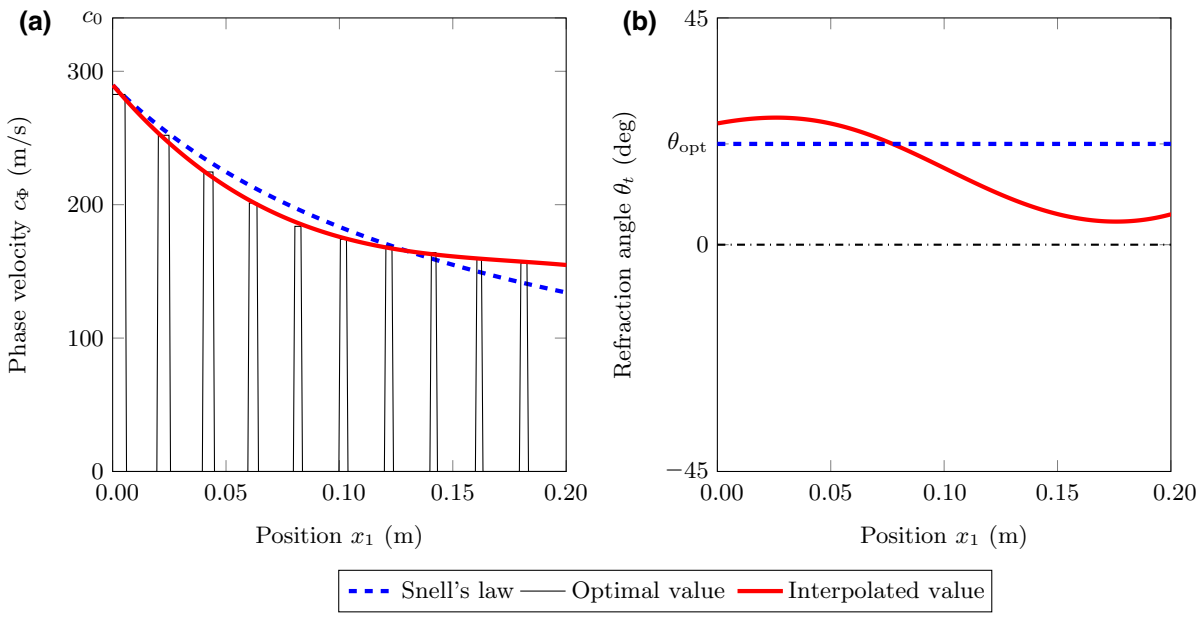

FIG. 6. Comparison of optimal sound speeds (a) and refraction angles (b) according to Snell's law (blue), from the explicit model (black), and from interpolation (red).

configuration ensures beam deflection while being relatively easy to manufacture using additive-manufacturing methods. The analytical and numerical results are in excellent agreement, as presented in Fig. 4(b), showing once again that the proposed explicit model is adapted to the modeling of acoustic metalenses for baffled sources.

VI. MATERIALS AND METHODS

While the FEM results validate the explicit modeling of acoustic metalenses, this section focuses on the experimental validation of the results. A sample having the optimal geometry is manufactured and tested in the controlled environment within the anechoic chamber of the Acoustic Laboratory of Le Mans University, seen in Figs. 5(a) and 5(b). The sample observed in Fig. 5(a) is manufactured by Stellantis by a fused-deposition-modeling process using the material ABS-M30 on a Stratasys Fortus 900mc printer. The total print time is approximately 60 h. The metalens is then mounted at the open end of a rectangular duct and baffled by a thick plate of plywood, as depicted in Fig. 5(b). On the other end of the duct, nine square loudspeakers generate a plane wave. The radiated pressure in the anechoic chamber is probed with a microphone.

The source signal is a linear sweep sine between frequencies $f_{\min} = 100$ Hz and $f_{\max} = 3000$ Hz. This signal is then amplified with an FX Audio high-fidelity class D amplifier (amplifier: NFJ&FXAUDIO FX502PRO), which powers the nine sources (arranged in a 3×3 square array) Tectonic TEBM36S12-4/A square BMR driver to generate a plane wave in the waveguide. The pressure field in the exterior domain is then measured on a 1000×1000 mm^2 region with a microphone mounted on a moving arm, and the results are averaged over 200 cycles. While the analytical model is two dimensional (meaning that the width along $\hat{\mathbf{e}}_3$ has no importance), the sample has depth $L_3 = w^{(0)} = 20$ cm. Hence, the resulting acoustic field is probed on the plane $\mathcal{H}$, as shown in Figs. 5(b) and 5(c). The pressure is probed with a 1/4-in. pressure-field microphone (B&K type 4135) with use of a preamplifier (B&K type 2670) with a B&K Nexus signal-conditioning module. The moving arm is controlled by two linear stages (Zaber 001-X-LRT1000AL-E08C) spanning the region $\mathcal{H}$ with an in-plane step $|\Delta\mathbf{x}| = 1$ cm. The pressure field is also evaluated along the curve $\mathcal{D}$ at a distance $d = 50$ cm from the center of the metalens and over 50 positions in the range $\theta \in [-\pi/2, \pi/2]$.

VII. RESULTS

The results of the two different models as well as the experimental data are presented in this section. First, the profiles of sound speed and refraction angle are shown and evidence the spatially dependent properties of the metalens. Then, the radiated pressure maps and normalized-near-field-angular-response results are presented for the optimized configuration.

A. Sound speed and angle of refraction

In this section, the optimal sound speed and refraction angles are investigated as if the couplings between the slits did not exist. For this purpose, the sound speed within the metalens is directly evaluated from the dispersion relation

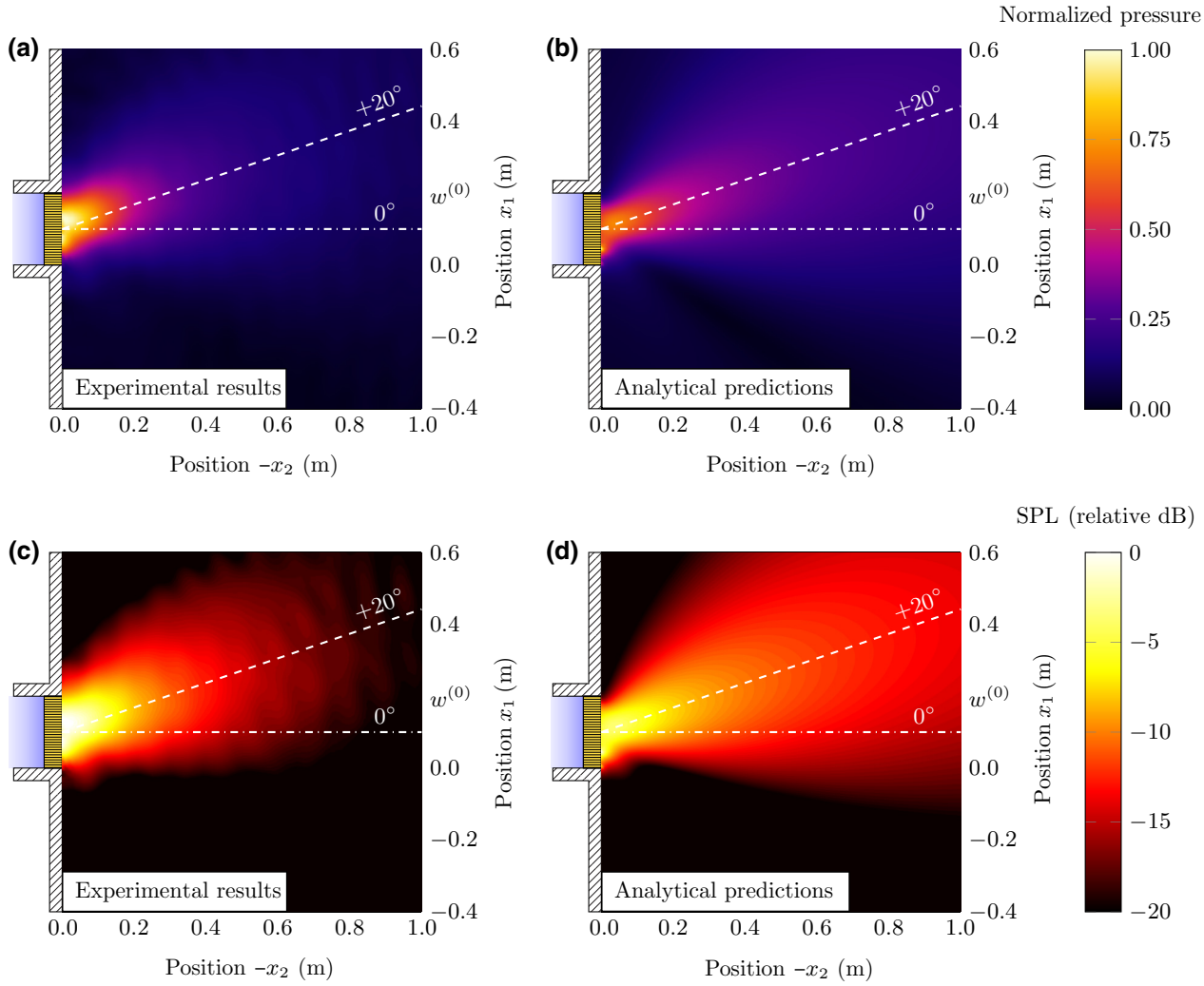

FIG. 7. Results for the metalens steering the acoustic beam by $\theta_{\text{opt}} = +20°$. (a),(b) Normalized acoustic pressure and (c),(d) SPL in the radiated domain $\Omega^{(\text{rad})}$ at frequency $f_{\text{opt}} = 2\,\text{kHz}$. (a),(c) Experimental results. (b),(d) Analytical predictions.

of the unit cell within each slit. The wave number $k^{(n)}$ in the nth slit satisfies $\cos(k^{(n)}L) = (1/2)\text{Tr}\left(\mathbf{T}^{(n)}\right)$, where Tr is the trace operator. Once calculated, the phase velocity in the slits takes the form $c_\Phi^{(n)} = \omega/\text{Re}\left(k^{(n)}\right)$. In this way the sound speed at the interface Γ_0 is given by

$$c_\Phi(x_1) = \begin{cases} c_\Phi^{(n)} & \text{for all } \mathbf{x} \in \Gamma_0^{(n)}, \\ 0 & \text{for all } \mathbf{x} \in \Gamma_0 \backslash \Gamma_0^{(n)}. \end{cases} \tag{15}$$

As the optimal sound speed is piecewise constant, estimation of the refraction angle from Eq. (2) has no physical meaning. The derivative $d(1/c_\Phi)/dx_1$ is either zero or $\pm\infty$ at the singularities (positions $x_1 = d^{(n)}$ and $x_1 = d^{(n)} + w^{(n)}$). Therefore, the profiles of the sound speed and the optimal refraction angle are interpolated and are shown in Fig. 6. Another approach is to estimate the profile of the sound speed knowing that the refraction angle is $\theta_{\text{opt}} = +20°$, again using Eq. (2). The derivation of the profile is trivial, and for a constant refraction angle the sound speed is given by

$$c_\Phi(x_1) = \left(\frac{x_1}{Lc_0}\sin(\pi/9) + \frac{1}{c_\Phi(0)}\right)^{-1}, \tag{16}$$

which is shown by the blue curve in Fig. 6. Both approaches, i.e., computing the sound-speed profile for a constant refraction angle and computing the refraction angle from the dispersion relation, give distinct results. On the one hand, we observe what the sound-speed profile should be if a constant refraction angle is desired. On the other hand, the effective profile of the refraction angle of the metalens is retrieved from the dispersion relation of the slits. Additional content is available in Supplemental Material [11].

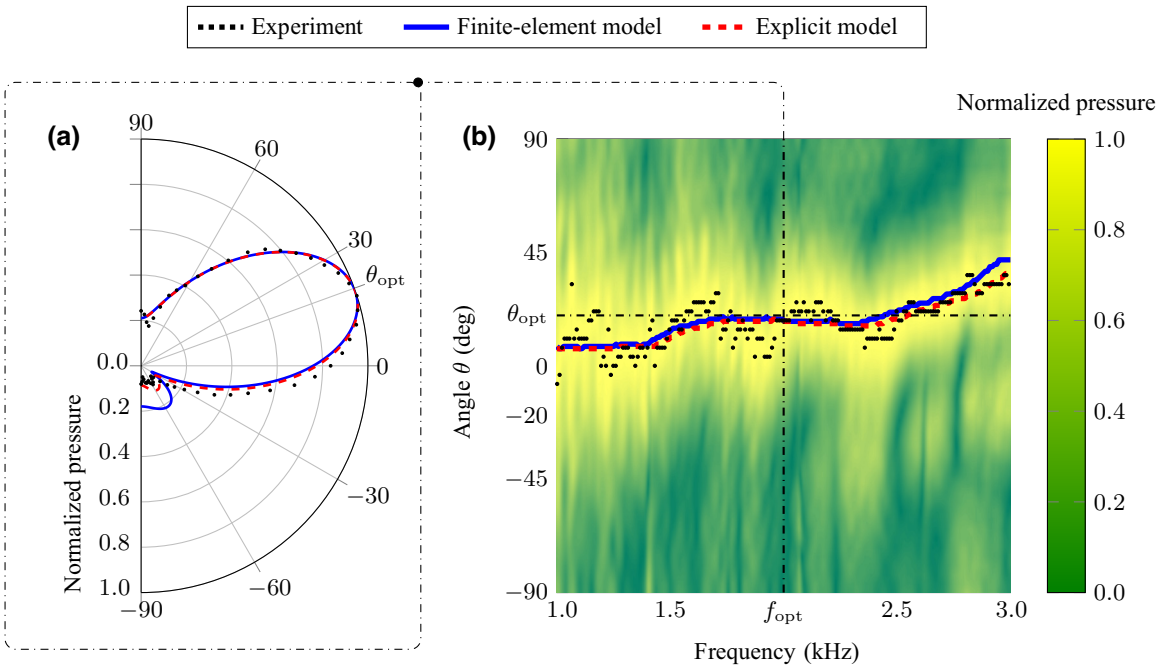

FIG. 8. (a) Normalized near-field angular response at frequency f_{opt} and (b) angle of maximal acoustic pressure with respect to frequency. Numerical and explicit results are shown as solid blue and dashed red lines, respectively, and experimental results as shown as dotted black lines.

B. Radiation and directivity

The metalens is optimized for the single frequency $f_{\text{opt}} = 2$ kHz, but experimental results are estimated over $N_{\text{f}} = 1800$ linearly spaced frequencies within the bounds $f_{\text{min}} = 1$ kHz and $f_{\text{max}} = 3$ kHz. While the far-field directivity is readily accessible from both the explicit model and the FEM, only the near-field acoustic pressure is measured experimentally. The results for the radiated acoustic pressure are presented here, and the normalized acoustic pressure $|p|/\max|p|$ and SPL are shown in Fig. 7.

We qualitatively observe good agreement between the experimental data and the radiated pressure predicted by the explicit model. However, the acoustic pressure seems to be lower experimentally, which is especially visible on the SPL fields in Figs. 7(c) and 7(d). This drop in amplitude is due to the metalens being infinite in the explicit model, i.e., the 2D model implies an infinite dimension in the out-of-plane direction $\hat{\mathbf{e}}_3$. In other words, while in the explicit model the pressure at any arbitrary point in $\Omega^{(\text{rad})}$ is the contribution of an infinite source along $\hat{\mathbf{e}}_3$, this source is only 20 cm deep in the experiment. Thus, a lower pressure amplitude (and a lower SPL) in $\Omega^{(\text{rad})}$ is expected to be observed experimentally. In addition, modes along $\hat{\mathbf{e}}_3$ are expected to emerge experimentally and to be located at the same frequencies as those in the $\hat{\mathbf{e}}_1$ direction because of the waveguide having a square cross section. This is demonstrated in Supplemental Material [11] by solving the full 3D problem with the FEM.

Besides, part of the incident energy reflected at Γ_{L} is then reflected onto the source itself, inevitably altering the incident field in $\Omega^{(0)}$. This effect is not accounted for in the present 2D model, but could be a topic of investigation in further studies. Still, the proposed metalenses have a high transmission coefficient, which means the part of the incident energy in $\Omega^{(0)}$ that is either absorbed or reflected is relatively low. This translates into the incident field being not significantly disturbed by the high-order reflections between the source and Γ_{L}. In Supplemental Material [11], it is shown that the transmission loss is very low, meaning almost the entirety of the incident field goes through the metalens. Moreover, the transmission coefficient of the metalens could also be maximized and set as an objective function during the optimization process.

Figure 8(a) shows the normalized near-field angular response at the frequency of optimization. Although the metalens is optimized for the single frequency f_{opt}, the effect of lensing is preserved across a wider frequency range. This is supported by the results presented in Fig. 8(b) over the range $f \in [f_{\text{min}}, f_{\text{max}}]$.

While both the FEM and the explicit model show very good agreement, the experimental data are not as smooth, although the general trend is preserved. This is evidenced when superimposing the angle-frequency map of normalized pressure obtained experimentally with the location of the angle of maximal pressure. Here again, this behavior is made possible by the regimes in which the resonant slits are operating and is linked to the configuration

of Helmholtz resonators, as evidenced in Supplemental Material [11].

VIII. CONCLUSIONS

In this work, the behavior of metalenses based on slits loaded with Helmholtz resonators is reported mathematically, numerically, and experimentally. The explicit model is developed in two dimensions, accounting for thermal and viscous losses, interslit couplings, and high-order modes in the baffled waveguide. In addition, the radiated pressure is estimated semianalytically via Green's integral formulations. The results of the explicit model are first validated against FEM solutions, and both show excellent agreement over multiple configurations and wide frequency ranges, above the cut-off frequency of the main duct.

The explicit model is then used as a kernel for an optimization procedure, providing metalenses with the optimal geometry for several selected targets, which focus or steer an acoustic beam. A sample having the optimal geometry is built by additive manufacturing and tested experimentally. The experimental results show good agreement with both the FEM and the analytical model, especially for the near-field angular response. While there are discrepancies regarding the absolute pressure in the experimental observations, which are mainly due to the system being finite and transverse modes, they are accurately predicted by the FEM with a 3D geometry.

Although the proposed explicit model has a fair number of advantages when compared with FEM solutions, limitations still exist. These limitations are mainly related to the truncation of infinite series and integrals, length corrections, and the inter-resonator couplings that may arise in some particular configurations. As previously mentioned, back-and-forth reflections between the source and the metalens are present but can be ignored in the case of low transmission loss.

Finally, the explicit model could be extended so as to account for 3D geometries as good agreement between the experimental data and the 3D FEM simulations is demonstrated. Additionally, the optimization routines could be adapted for multifrequency cases and further developed for faster minimization times. These improvements would provide an even-more-robust and even-more-comprehensive tool for the modeling and design of acoustic metalenses and more generally 3D metamaterials.

The data that support the findings of this study are available as Supplemental Material [11].

ACKNOWLEDGMENTS

This research was funded by Stellantis. J.-P.G. and V.R.-G, also acknowledge the support of the ANR-RGC METARoom project (ANR-18-CE08-002).

CREDIT AUTHORSHIP CONTRIBUTION STATEMENT

T.C. has worked on methodology, software, validation, formal analysis, investigation, resources, data curation, writing—original draft, writing—review & editing, and visualization. V.R.-G. and J.P.G. both contributed to conceptualization, methodology, validation, formal analysis, investigation, resources, data curation, writing—review & editing, and supervision. M.M. was in charge of the conceptualization, methodology, validation, formal analysis, investigation, resources, writing—review & editing, supervision, project administration, and funding acquisition. J.-C.C. was involved on conceptualization, resources, supervision, and project administration.

[1] T. Betlehem, W. Zhang, M. A. Poletti, and T. D. Abhayapala, Personal sound zones: Delivering interface-free audio to multiple listeners, IEEE Signal. Process. Mag. **32**, 81 (2015).

[2] J. Cheer, PhD thesis, University Of Southampton, Southampton, 2012.

[3] S. J. Elliott and M. Jones, An active headrest for personal audio, J. Acoust. Soc. Am. **119**, 2702 (2006).

[4] X. Liao, J. Cheer, S. Elliott, and S. Zheng, Design of a loudspeaker array for personal audio in a car cabin, J. Audio Eng. Soc. **65**, 226 (2017).

[5] L. Vindrola, M. Melon, J.-C. Chamard, and B. Gazengel, Use of the filtered-x least-mean-squares algorithm to adapt personal sound zones in a car cabin, J. Acoust. Soc. Am. **150**, 1779 (2021).

[6] J. Lan, Y. Li, Y. Xu, and X. Liu, Manipulation of acoustic wavefront by gradient metasurface based on Helmholtz resonators, Sci. Rep. **7**, 10587 (2017).

[7] Y. Li, S. Qi, and M. Badreddine Assouar, Theory of metascreen-based acoustic passive phased array, New J. Phys. **18**, 043024 (2016).

[8] M. Amin, O. Siddiqui, M. Farhat, and A. Khelif, A perfect Fresnel acoustic reflector implemented by a Fano-resonant metascreen, J. Appl. Phys. **123**, 144502 (2018).

[9] M. Amin, O. Siddiqui, W. Orfali, M. Farhat, and A. Khelif, Resonant Beam Steering and Carpet Cloaking Using an Acoustic Transformational Metascreen, Phys. Rev. Appl. **10**, 064030 (2018).

[10] V. Dubos, A. Khettabi, D. H. Keefe, C. J. Nederveen, and A. C.. Pijnacker, Theory of sound propagation in a duct with a branched tube using modal decomposition, Acta Acust. **85**, 18 (1999).

[11] See Supplemental Material at http://link.aps.org/supplemental/10.1103/PhysRevApplied.20.024012 for more details on the calculations.

[12] P. Benner, A. Cohen, M. Ohlberger, and K. Willcox, editors, *Model reduction and approximation: theory and algorithms* (SIAM J. Appl., Philadelphia, 2017).

[13] J. Kennedy and R. Eberhart, in *Proceedings of ICNN'95—International Conference on Neural Networks* (IEEE, Perth, WA, Australia, 1995), vol. 4, p. 1942.

[14] M. E. H. Pedersen and A. J. Chipperfield, Simplifying particle swarm optimization, Appl. Soft Comput. **10**, 618 (2010).
[15] C. Kai C., K. F. Leong, and C. S. Lim, *Rapid Prototyping: Principles and Applications, 2nd Edition* (World Scientific, New Jersey, 2003).
[16] T. Grimm, *User's Guide to Rapid Prototyping* (SME, Dearborn, MI, 2004).
[17] M. Born and E. Wolf, *Principles of Optics* (Cambridge University Press, Cambridge, UK, 2019).
[18] Y. Xie, W. Wang, H. Chen, A. Konneker, B.-Ioan Popa, and S. A. Cummer, Wavefront modulation and subwavelength diffractive acoustics with an acoustic metasurface, Nat. Commun. **5**, 5553 (2014).
[19] B. Brouard, D. Lafarge, and J.-F. Allard, A general method of modelling sound propagation in layered media, J. Sound Vib. **183**, 129 (1995).
[20] R. A. Horn and C. R. Johnson, *Matrix Analysis* (Cambridge University Press, New York, NY, 2017), 2nd ed.
[21] M. C. Pease, *Methods of Matrix Algebra* (Elsevier NetLibrary, Incorporated, New York, Boulder, 1965).
[22] W. H. Press, *Numerical Recipes: The Art of Scientific Computing* (Cambridge University Press, Cambridge, UK, New York, 2007), 3rd ed.
[23] A. N. Stroh, Steady state problems in anisotropic elasticity, J. Math. Phys. **41**, 77 (1962).
[24] J. Kergomard and A. Garcia, Simple discontinuities in acoustic waveguides at low frequencies: Critical analysis and formulae, J. Sound. Vib. **114**, 465 (1987).
[25] M. R. Stinson, The propagation of plane sound waves in narrow and wide circular tubes, and generalization to uniform tubes of arbitrary cross-sectional shape, J. Acoust. Soc. Am. **89**, 550 (1991).
[26] S. H. Schot, Eighty years of Sommerfeld's radiation condition, Hist. Math. **19**, 385 (1992).
[27] A. Sommerfeld, *Partial Differential Equations in Physics*, Lectures on Theoretical Physics (Academic Press, New York, 1964).
[28] J.-P. Berenger, A perfectly matched layer for the absorption of electromagnetic waves, J. Comput. Phys. **114**, 185 (1994).
[29] E. G. Williams, *Fourier Acoustics: Sound Radiation and Nearfield Acoustical Holography* (Academic Press, San Diego, CA, 1999).
[30] J. A. Nelder and R. Mead, A simplex method for function minimization, Comput. J. **7**, 308 (1965).
[31] F. N. Fritsch and R. E. Carlson, Monotone piecewise cubic interpolation, SIAM J. Numer. Anal. **17**, 238 (1980).
[32] F. Bloch, Über die Quantenmechanik der Elektronen in Kristallgittern, Z. Phys. **52**, 555 (1929).
[33] M. Bruneau, *Fundamentals of Acoustics* (ISTE Ltd, London; Newport Beach, CA, 2006).
[34] J.-P. Groby, W. Huang, A. Lardeau, and Y. Aurégan, The use of slow waves to design simple sound absorbing materials, J. Appl. Phys. **117**, 124903 (2015).
[35] J.-P. Groby, R. Pommier, and Y. Aurégan, Use of slow sound to design perfect and broadband passive sound absorbing materials, J. Acoust. Soc. Am. **139**, 1660 (2016).
[36] J.-P. Groby, PhD thesis, Université de la Méditerranée - Aix-Marseille II, Marseille, 2005.
[37] V. Romero-García, N. Jiménez, J.-P. Groby, A. Merkel, V. Tournat, G. Theocharis, O. Richoux, and V. Pagneux, Perfect Absorption in Mirror-Symmetric Acoustic Metascreens, Phys. Rev. Appl. **14**, 054055 (2020).